Journal name

DOI:10.1177/09544062221080139

MULTIPLE BALLISTIC IMPACTS OF THIN METALLIC PLATES: NUMERICAL SIMULATION

Journal:	*Part C: Journal of Mechanical Engineering Science*
Manuscript ID	JMES-21-2383.R1
Manuscript Type:	Original Research Article
Date Submitted by the Author:	12-Jan-2022
Complete List of Authors:	Qiang, Lusheng; Nanjing University of Aeronautics and Astronautics, Zhang, Rui; Xi'an Jiaotong University, Zhao, Chunzheng; Nanjing University of Aeronautics and Astronautics, Ren, Jianwei; Nanjing University of Aeronautics and Astronautics, Ni, Changye; Nanjing University of Aeronautics and Astronautics, Zhao, Zhenyu; Nanjing University of Aeronautics and Astronautics, Lu, Tian; Nanjing University of Aeronautics and Astronautics, State Key Laboratory of Mechanics and Control of Mechanical Structures
Keywords:	Multiple impacts, Ballistic limit, Failure modes, Metallic plate, Finite element simulation
Abstract:	The ballistic performance of protective structures under multiple projectile impacts attracts increasing attention due to its practical importance, and existing studies were seldomly devoted to exploring how the structure would deform and fail when subjected to such loads. This study aimed to characterize the multi-hit ballistic resistance of fully-clamped thin plates made of 304 stainless steel using finite element method, with the equivalent plastic strain employed to define material damage and failure/fracture. The numerical model was validated against existing experimental results of double impacts at the same location, with good agreement achieved. The model was subsequently employed to quantify the effects of impact position, interval time between successive hits, projectile nose shape (e.g., spherical, flat and conical), and boundary condition of target plate on ballistic limit and deformation/failure modes. Further, ballistic limit boundaries were constructed for both double and triple impacts of projectiles. Obtained results are helpful for designing high-performance protective structures against multiple projectile impacts.
Note: The following files were submitted by the author for peer review, but cannot be converted to PDF. You must view these files (e.g. movies) online.	
Figures for JMES-21-2383.R1.rar	

MULTIPLE BALLISTIC IMPACTS OF THIN METALLIC PLATES: NUMERICAL SIMULATION

Lu-sheng Qiang [1,2], Rui Zhang [2,3,*], Chun-zheng Zhao [1,2], Jian-wei Ren [1,2],

Chang-ye Ni [1,2], Zhen-yu Zhao [1,2,*], Tian Jian Lu [1,2]

[1] *State Key Laboratory of Mechanics and Control of Mechanical Structures, Nanjing University of Aeronautics and Astronautics, Nanjing 210016, China*

[2] *MIIT Key Laboratory of Multifunctional Lightweight Materials and Structures (MLMS), Nanjing University of Aeronautics and Astronautics, Nanjing 210016, China*

[3] *School of Aerospace, Xi'an Jiaotong University, Xi'an 710049, China*

---

*Corresponding author.

E-mail address: zr19950122@163.com (R. Zhang), zhenyu_zhao@nuaa.edu.cn (Z.Y. Zhao).

Lu-sheng Qiang, qianglusheng@nuaa.edu.cn

Rui Zhang, zr19950122@163.com

Chun-zheng Zhao, zcz1998@nuaa.edu.cn

Jian-wei Ren, renjian0621@163.com

Chang-ye Ni, cyni@nuaa.edu.cn

Zhen-yu Zhao, zhenyu_zhao@nuaa.edu.cn

Tian Jian Lu, tjlu@nuaa.edu.cn

MULTIPLE BALLISTIC IMPACTS OF THIN METALLIC PLATES: NUMERICAL SIMULATION

Abstract

The ballistic performance of protective structures under multiple projectile impacts attracts increasing attention due to its practical importance, and existing studies were seldomly devoted to exploring how the structure would deform and fail when subjected to such loads. This study aimed to characterize the multi-hit ballistic resistance of fully-clamped thin plates made of 304 stainless steel using finite element method, with the equivalent plastic strain employed to define material damage and failure/fracture. The numerical model was validated against existing experimental results of double impacts at the same location, with good agreement achieved. The model was subsequently employed to quantify the effects of impact position, interval time between successive hits, projectile nose shape (e.g., spherical, flat and conical), and boundary condition of target plate on ballistic limit and deformation/failure modes. Further, ballistic limit boundaries were constructed for both double and triple impacts of projectiles. Obtained results are helpful for designing high-performance protective structures against multiple projectile impacts.

Keywords: Multiple impacts; Ballistic limit; Failure modes; Metallic plate; Finite element simulation

1. Introduction

Often, protective structures need to endure multiple ballistic impacts, e.g., personnel armors and military fortifications subjected to continuous firing from automatic weapons[1,2], civil/military vehicles hit by blast fragment cluster from shallow-buried mines[3,4], and spacecrafts/satellites under hypervelocity impact of debris cloud[5]. At present, while many previous studies[6-10] alluded to the importance of multiple ballistic impact loads, few attempted to systematically explore how a structure would deform and fail when subjected to such loads. Different from multiple ballistic impacts, multiple (repeated) impact loadings with low impact velocity and relatively large interval time have been extensively investigated. In this case, structural fracture would not occur, and the transverse displacement of structure could be predicted by static analysis, which is known as pseudo-shakedown[11,12]. Further, upon enduring the initial ballistic impact, the structure would typically suffer from large deformation and damage, and hence how it would perform under ballistic impact(s) is of importance for practical protective design.

Existing studies of multiple ballistic impacts targeted mainly fiber-reinforced composites[13-17] and ceramic/metal armors[18-21]. For instance, multiple ballistic impacts of fragment simulating projectile on S-2 glass/SC15 laminates were investigated, both numerically[13] and experimentally[14]. The initial impact damage was found to extend towards the supporting edges of the laminate, resulting in about 4.5% and 9% decrease in multi-hit ballistic limit velocity and energy absorption, respectively. In another study, with simultaneous and sequential firing of projectiles achieved by light-gas gun, it was found that, compared with simultaneous impact, sequential impact on S2-glass/epoxy laminate led to 10% increase in energy absorption and 18% enlargement in delamination area.[15] Further, the dependence of the back deflection of ultra-high molecule weight polyethylene laminates upon the number of ballistic impacts was investigated.[16,17] On the other hand, under multiple ballistic impacts from standardized bullets, ceramic composite armors with polyurethane resin adhesive employed for interfacial bonding exhibited less adhesive layer failure and ceramic debonding than those bonded using epoxy.[18,19]

In addition to fiber-reinforced composite laminates, the multi-hit ballistic performance of ceramic/metal bi-layer mosaic armors was evaluated in terms of probability of protection.[20] The present authors used a combined experimental and numerical approach to investigate the ballistic behaviors of ceramic/metal bi-layer mosaic armors as well as metallic honeycomb enhanced mosaic armors.[21] Special focus was placed upon quantifying the influence of ceramic tile size, impact position, border-effect and inter tile gap width on single and multiple ballistic impact resistance. It was demonstrated that, relative to monolithic ceramic armor and traditional bi-layer mosaic armor, the honeycomb enhanced mosaic armor could efficiently localize the extent of damage after the first strike and maintain effective bonding between adjacent ceramic tiles and the back metallic plate, thus enabling balanced single and multiple impact resistance.[21] In a separate study, a novel sandwich plate having metallic pyramidal lattice truss core with ceramic prism insertions and epoxy resin filling the void spaces was constructed, and its impact responses and ballistic resistance were evaluated.[22] The ballistic limit velocity, energy absorption and failure mechanisms were systematically investigated, both numerically and experimentally. The proposed hybrid-cored sandwich construction exhibited excellent ballistic performance under single and multiple ballistic impacts, with the back face-sheet playing a more significant role than the front face-sheet in resisting ballistic impacts.[22]

The ballistic performance of a bi-layer construction comprising a stainless steel plate glued onto a carbon fiber-reinforced composite laminate plate was characterized experimentally.[23] Both single and double impacts (*at the same location*) by a steel ball were considered, and the ballistic performance was compared with monolithic stainless steel plate and monolithic composite laminate plate having identical area mass. As shown in Figure 1, with the initial velocity denoted by V_I and subsequent velocity by V_{II}, the ballistic performance of the target could be characterized by introducing the V_I-V_{II} space and the ballistic limit boundary separating the perforation and non-perforation regimes; further, the double-impact resistance could be quantified by defining the equivelocity ballistic limit velocity V_{2L}.[23] Subsequently, these experimental results of both single and double impacts were reproduced using the method of finite elements (FE).[24] Built upon the geometric intervals method[25], two (non-contacting) projectiles were constructed in the FE model such that multiple impacts at the same location of the target plate could be realized by tailoring the position of one projectile relative to other projectiles.[24] Nonetheless, in terms of computational efficiency, such numerical methodology is suitable for the case when the spatial distance intervals between successive projectiles are relatively small, such as blast fragment cluster[26].

The studies cited above only considered multiple impacts at fixed impact locations and did not consider the variation in impact position. Further, how the interval time between successive impacts, projectile morphology (nose shape), multiple impacts at different locations, and boundary condition affects the ballistic performance of the target plate remains elusive. This study aimed to address these issues using FE simulations. For validation, the simulation results were compared with existing experimental data and FE results. To improve the computational efficiency, the method of full-restart was employed in lieu of the geometric intervals method. Further, triple ballistic impacts at the same location were carried out to extend the ballistic limit boundary of Figure 1 to ballistic limit surface. The paper was organized as follows. Section 2 introduced the problem of multiple ballistic impacts. Section 3 described FE simulation settings, determination of material parameters, and validation of simulation results. Section 4 presented the simulated multi-hit ballistic responses of stainless steel plates, explored the underlying physical mechanism, and discussed the effects of impact position, interval time between successive impacts, projectile nose shape, and boundary condition of target plate. Finally, according to the simulation results of triple impacts, the ballistic limit surface in V_I-V_{II}-V_{III} space was constructed.

2. The problem of multiple ballistic impacts

As shown in Figure 2(a), let subscripts "I" and "II" denote separately projectile I and projectile II, which have initial velocity V_I and V_{II}, respectively. In accordance with the impact tests reported in previous studies[23,24], the projectiles were taken as rigid spheres, each having a diameter of 12.7 mm and a mass of 8.3 g, while the target plate was a thin circular disc made of 304 stainless steel (SS), fully clamped around its edges. A series of FE simulations of double ballistic impacts at the same location on the target were performed. To validate the present FE model, the results were compared with existing experimental and numerical results.

The validated FE model was subsequently employed to carry out the following tasks:

i) To study the effect of sequential impacts at different locations on ballistic performance of the target plate, spherical projectile I impacting at plate center was maintained, while the impact location of spherical projectile II was shifted from plate center by d = 0 mm, 12.7 mm, and 25 mm, respectively; the interval time Δt between projectiles I and II was fixed at 1000 μs.

ii) For spherical projectiles, with the shift of impact location d fixed at 12.7 mm, Δt was varied to quantify the effect of interval time.

iii) Double impacts at the same location with projectiles having different projectile nose shapes (i.e., sphere, flat, and cone) but fixed mass and diameter were considered, as shown in Figure 2(b), with Δt = 1000 μs.

iv) To study the effect of boundary condition on ballistic performance, double impacts (at the same location; Δt = 1000 μs; spherical projectiles) of fully-fixed disc, fully-fixed square, and oppositely-fixed square having the same effective impacted area were investigated, as shown in Figure 2(c).

v) Triple impacts (Δt = 1000 μs) at the same location were performed.

Note that, in the current study, only normal impacts were considered, i.e., the projectiles were perpendicular to the target plate.

3. Numerical simulations

3.1 Finite element model

For the tasks described in the previous section, numerical simulations were performed using the commercially available FE code LS-DYNA. As shown in Figure 3, the 304 SS target plate, fully-clamped at its edges, had a diameter of 100 mm and a thickness of 0.71 mm, same as those reported in previous studies[23,24]. Constant stress solid elements (Solid 164) were used to establish the FE model. To ensure numerical convergence, finer meshes (element size ~ 0.178 mm × 0.178

mm × 0.178 mm) were employed for the central area of the plate where impacts took place while, outside this region, the mesh size in plane was gradually increased along the radial direction of the disk (mesh size in thickness fixed at 0.178mm). The projectile was meshed with an element size of ~ 0.5 mm × 0.5 mm × 0.5 mm. Such meshing was consistent with the results of mesh sensitivity study reported.[24]

In the present study, the damping effect was applied to the target plate to mimic the actual impact experiment[23] such that the plate after impact could quickly approach a stable equilibrium state[27]. Specifically, the method of mass-weighted nodal damping was adopted wherein the damping factor was calculated from the first-order natural frequency of the target plate.[28] Contact between the impacting projectiles and the target plate was defined as ERODING_SURFACE_TO_SURFACE, with penalty contact formulation adopted and the dynamic coefficient of friction specified as 0.57[24].

The method of full-restart was adopted to simulate multiple ballistic impacts. For each new impact, a full restart was activated: the previous projectile was deleted such that a new projectile could be added, and the "d3dump" database (containing deformation, stress and strain fields in target plate) obtained at the end of the previous ballistic impact were used to carry out the new impact via *STRESS_INITIALIZTION. However, when investigating the influence of interval time between sequential impacts on ballistic performance, the method of geometric intervals was employed: the two projectiles were established at one step, with the interval time tailored by varying the distance between the projectiles.

3.2 Constitutive models

As previously mentioned, the projectiles were regarded as rigid bodies with a density of 7778 kg m^{-3}. The constitutive behavior of 304 SS was described using the Johnson-Cook model[29], while the strain rate effect was characterized using the Cowper-Symonds model[30]. The dynamic stress was thence written as:

$$\sigma_D = \left[A + B\left(\bar{\varepsilon}^{\mathrm{pl}}\right)^n\right]\left[1 + \left(\frac{\bar{\varepsilon}^{\mathrm{pl}\prime}}{C}\right)^{\frac{1}{P}}\right]\left[1 - \left(\frac{T - T_{\mathrm{r}}}{T_{\mathrm{m}} - T_{\mathrm{r}}}\right)^m\right], \qquad (1)$$

where A, B, n and m were material constants, $\bar{\varepsilon}^{\mathrm{pl}}$ was the equivalent plastic strain, T was the actual temperature, T_{r} and T_{m} was the room and melting temperature, respectively, C and P were the parameters governing strain rate effect, and $\bar{\varepsilon}^{\mathrm{pl}\prime}$ was the actual plastic strain rate. As shown in Figure 4, relevant values of A, B, n, C, P were fitted from the experimental results of 304 SS reported[23,24,30], and were listed in Table 1.

The failure and fracture of 304 SS were based on damage evolution wherein damage of the material was assumed to occur, and the corresponding elements were removed when the damage parameter D exceeded unity. The damage parameter D was defined as:

$$D = \sum\left(\frac{\Delta\bar{\varepsilon}^{\mathrm{pl}}}{\bar{\varepsilon}_{\mathrm{f}}^{\mathrm{pl}}}\right), \qquad (2)$$

where $\Delta\bar{\varepsilon}^{\mathrm{pl}}$ and $\bar{\varepsilon}_{\mathrm{f}}^{\mathrm{pl}}$ were the increment of equivalent plastic strain and the strain at fracture, respectively. Once the plastic strain accumulated in all incremental steps of an element reached the fracture strain, the element was directly removed (without stiffness degradation[31]). Further, $\bar{\varepsilon}_{\mathrm{f}}^{\mathrm{pl}}$ was given by:

$$\bar{\varepsilon}_{\mathrm{f}}^{\mathrm{pl}} = \left[D_1 + D_2 \exp\left(D_3\sigma^*\right)\right]\left[1 + D_4 \ln\left(\frac{\bar{\varepsilon}^{\mathrm{pl}\prime}}{\varepsilon_0'}\right)\right]\left[1 + D_5\left(\frac{T - T_{\mathrm{r}}}{T_{\mathrm{m}} - T_{\mathrm{r}}}\right)\right], \qquad (3)$$

where σ^* was the stress triaxiality, and D_1-D_5 were the failure parameters. Values of these failure parameters for 304 SS were taken,[32] and listed in Table 1.

3.3 Validation of numerical simulations

The present numerical simulations were validated against existing experimental results[23] and numerical results[24] for double impacts of spherical projectiles at the same location on clamped 304 SS circular disks. As shown in Figure 5, the predicted ballistic limit boundary in V_I-V_{II} space matched closely to those obtained experimentally[23] and numerically[24]. It was seen that the ballistic limit boundary was approximately linear in each of the two regions labeled as A and B, consistent with existing results[23,24]. Note that the numerical verification was based on Δt = 1000 μs, and the effect of Δt was discussed later in Section 4.2.

The endpoints of the ballistic limit boundary shown in Figure 1 represented the ballistic limit velocity V_L for single impact, while the intersection of this boundary with the trajectory $V_I = V_{II}$ defined the equivelocity ballistic limit velocity V_{2L} for double impacts at the same location. Quantitative comparisons of V_L and V_{2L} were presented in Table 2, and it was seen that the percentage errors of the present FE simulation relative to existing experimental results were less than 5%. Moreover, as shown in Figure 6, the failure modes predicted by the present FE simulation agreed fairly well with those from experiment[23] and simulation[24]. Specifically, the present simulation successfully captured circumferential cracking after significant bulging when the clamped plate was impacted at just below V_L in single impact, as well as secondary radial fracture after plugging when the plate was impacted at just below V_{2L} in double impacts. Therefore, the feasibility and validity of the numerical model developed in the present study was established.

4. Results and discussions

4.1 Impact location

The effect of impact location on ballistic performance was studied by impacting the center of target plate with projectile I, followed by impacting with projectile II at selected offset locations: d = 0 mm, 12.7 mm, and 25 mm. Both projectiles were spheres and the interval time between hits I and II was fixed at Δt = 1000 μs. The calculated ballistic limit boundaries were displayed in Figure

7(a), while corresponding deformation profiles and failure/fracture modes were presented in Figure 8(e). It was seen that, with the initial impact velocity V_I fixed, the ballistic limit velocity of second impact increased with increasing offset position *d*. When the offset *d* was sufficiently large, the ballistic limit velocity of second impact would approach the single-impact ballistic limit of V_L = 206.3 m s^{-1}, causing the ballistic limit boundary to become nearly horizontal. For clarity, the three points located at the upper left corner of Figure 7(a) were enlarged to compare the single impact performance at different locations. It was shown that the target was easier to be perforated closer to its boundary.[33,34]

The residual velocity of projectile II impacting at different offset locations was presented in Figures 7(b) and (c) for V_I = 120 m s^{-1} and 220 m s^{-1}, respectively. Increasing the V_I caused obvious shifting of the residual velocity curve toward the left if *d* = 12.7 mm, thus reduced ballistic resistance. However, if the offset was increased to *d* = 25 mm, the ballistic resistance was almost not affected as no obvious shifting of the residual velocity curve was observed. This was understandable, as in the former case, 12.7 mm was also the diameter of the spherical projectile, so that the damage caused by the second projectile complemented that caused by the first projectile, thus leading to severe damage (Figure 8(e)) and inferior ballistic resistance. In contrast, in the case of *d* = 25 mm, the damage zones of the two separate impacts did not overlap, as shown clearly in Figure 8(e), so that the offset had little influence on ballistic resistance.

In Figure 7(d), the residual velocity of projectile II was plotted as a function of its impact time for varying offset but fixed V_I (=120 m s^{-1}), where V_Z and V_X represented the velocity of the projectile perpendicular to and along the radial direction of the target plate, respectively. When projectile II hit at the center of the target, same as projectile I, it perforated the target, with quickly dropped velocity. In contrast, when projectile II hit at an offset location, the saucer-like deformation profile of the target plate caused by projectile I forced projectile II to exhibit a velocity component along the radial direction, i.e., V_X, albeit relatively small. As shown in Figure 8(a), after the impact by projectile I, local inclination of the target plate at the location of d = 12.7 mm was larger than that at d = 25 mm, such that the radial velocity of projectile II was larger in the former case than that in the latter. Note that, the negative value of V_X indicated that projectile II moved somewhat toward the axis of the target plate after it impacted the target, either at d = 12.7 mm or 25 mm.

The effect of impact location was mainly attributed to the accumulation and evolution of effective plastic strain, for it had been widely used to characterize material ductility damage as defined in Eq. (2). Figure 8(a) presented the effective plastic strain contour of target plate at the end of the first impact (V_I = 120 m s^{-1}) but before the second impact initiated, i.e., t_{II} = 0 μs. Subsequently, as the plate was impacted by projectile II at varying locations, Figures 8(b) ~ (d) displayed separately the evolution of effective plastic strain in the plate for d = 0, 12.7 and 25 mm. It was seen that, as the initial effective plastic strain was the largest when d = 0 mm, second impact at the identical location was the easiest and fastest route for the plate to fail, accompanied with the lowest ballistic limit velocity of second impact. Simultaneously, because the double impacts at d = 0 mm were axial-symmetrical, the distribution of effective plastic strain in Figure 8(b) remained also axial-symmetrical during the entire impacting process, with double peaks. Accordingly, the plate failed first at the two peaks, exhibiting a plug-type failure at the same positions as shown in Figure 8(e). As the impact location of projectile II was shifted from the target center to d = 12.7 and 25 mm, the curves of effective plastic strain were increasingly shifted away from the target center, as shown in Figures 8(c) and (d). In addition, corresponding to the shifting, the peaks of the curve also trended to move to the central area of the plate, resulting in its tearing and petalling failure in the case of d = 12.7 mm, as shown in Figure 8(e). Such trend was attributed to the lateral movement of projectile II (Figure 7(d)) due to the inclination of the plate after the impact by projectile I (Figure 8(a)). As previously discussed, when projectile II (diameter 12.7 mm) hit the target at the location of d = 12.7 mm, the resulting effective plastic strain interacted closely with that left by projectile I (diameter 12.7 mm) hitting the target center. The accumulated effective plastic strain at the impact location (d = 12.7 mm, Figure 8(c)) was significantly larger than that in the case of d = 25 mm, and hence the extent of damage and failure was much more severe in the case of d = 12.7 mm, as shown in Figure 8(e). Correspondingly, the ballistic limit velocity of second impact was lower.

4.2 Interval time between first and second impacts

In this section, the effect of interval time (Δt) between the first and second impacts on ballistic performance was investigated for the case of d = 12.7 mm, with no collision between projectiles I and II considered. Figure 9(a) plotted the evolution of deflection at the center of the clamped plate after it was impacted by projectile I with a velocity of 120 m s^{-1}. At 258 μs, the deflection reached a peak and the plate began to oscillate reciprocally: that is, the plate started to spring back from the peak deflection as part of the kinetic energy of projectile I was transferred as elastic deformation energy stored in the plate, thus enabling the plate to spring back once its deflection peaked. Accordingly, the dynamic response of the plate during projectile I impact could be divided into the bulge phase (0 ~ 258 μs) and the springback phase (> 258 μs). Figure 9(b) displayed the deformation process of the plate during the bulge phase. Upon impacting by projectile I, the plate started local bulging in a few microseconds. Subsequently, bending plastic hinges were formed and started to propagate toward the clamped boundary. During this phase, as the deflection at the plate center was further increased, the central impact area of the plate experienced membrane stretching from surrounding material. The whole plate was subjected to membrane stretching when the plastic hinges reached its clamped boundary, causing a saucer-like deformation profile as shown in Figure 9(b). During the springback phase, the deflection of the plate oscillated reciprocally with gradually decreasing magnitude due to damping, eventually reaching a steady state wherein the deflection became permanent. In terms of the interaction between projectile I and the clamped plate, the dynamic response could be divided into the coupling response phase and the free response phase. Figure 9(a) plotted the contact force between projectile I and the plate as a function of impact time.

It was seen that, during the coupling response phase, the contact force increased rapidly upon impacting, reaching a peak, and then dropped sharply, followed by oscillation. At 334.5 μs, the contact force became zero, and projectile I broke away from the target plate such that the plate entered the completely free response wherein dynamic springback occurred.

To quantify the effect of interval time on ballistic performance, the residual velocity of projectile II was presented in Figure 10(a) for varying interval time between first and second impacts, with V_I = 120 m s^{-1} and V_{II} = 220 m s^{-1}. Note that immediately before the plate was hit by projectile II, its deformation profile induced by projectile I was displayed in Figure 9(a). It was seen from Figure 10(a) that, when Δt = 0 μs, the residual velocity of projectile II was the lowest, implying that the target plate had the best ballistic resistance when projectiles I and II hit it simultaneously. As Δt was gradually increased, the target plate experienced increasingly large deformation before projectile II started impacting and, as a result, the residual velocity of projectile II increased nearly linearly. When Δt was increased to 64.5 μs, the residual velocity was increased to 150 m s^{-1}. However, further increasing Δt did not lead to a significant increase in residual velocity: from 150 m s^{-1} to 162 m s^{-1} when Δt was 258 μs. Subsequently, as the moving direction of projectile II was not consistent with the oscillating direction of the target plate, its residual velocity fluctuated; Figure 10(a).

Figure 10(b) displayed ballistic limit boundaries corresponding to Δt = 0 μs, 32 μs and 1000 μs. When Δt = 0 μs, the ballistic limit velocity of projectile II at d = 12.7 mm slightly increased with increasing V_I. This could be attributed to the fact that, when subjected to simultaneous impacting of projectiles I and II, it is easier for the target plate to deform globally such that local failure at location d = 12.7 mm became more difficult. However, the variation trend was reversed when Δt was increased to 32 μs or 1000 μs, i.e., the ballistic limit velocity of second impact decreased, nearly linearly, with increasing V_I; Figure 10(b). Further, with V_I fixed, the ballistic limit velocity of projectile II decreased with increasing Δt.

4.3 Projectile nose shape

To explore how projectile nose shape affects multi-impact ballistic resistance, projectiles having conical and flat noses were considered in addition to spherical projectiles, as shown in Figure 2(b). For illustration, all projectiles had identical mass and diameter, with d = 0 mm (i.e., no offset in impact locations) and Δt = 1000 μs. To avoid instability of numerical calculations, a small portion of the sharp conical nose was cut off such that its front had a circular cross-section, whose diameter was one-tenth the projectile diameter (12.7 mm). Figure 11(a) presented the residual velocity of projectile I having varying nose shape for the case of single impact, from which it was seen that the ballistic limit velocity V_L decreased if the nose shape of projectile I was varied from sphere to flat and then from flat to cone. In Figure 12(a), for single impact, the effect of projectile nose shape upon deformation and failure modes was presented, with V_I = 120 m s^{-1}. A flat projectile caused severe shearing in the localized region of the plate where it met with the sharp edge of the flat projectile, while the plate as a whole experienced membrane stretching. Accordingly, as shown in Figure 12(a), plugging failure was easier to occur when the plate was hit by a flat projectile in lieu of a spherical one, thus it had a lower ballistic resistance to the flat projectile. In comparison with spherical and flat projectiles, due to the more concentrated action of a conical nosed impactor on the plate during the bulge phase, the conical projectile led to the severest localized deformation, causing petalling failure and hence the least ballistic resistance; Figure 12(a). It should be noted that the current result is limited to thin 304 SS plates that are prone to plastic bulging and membrane stretching. If the target plate is thicker or made of other metallic sheets, the order of nose shapes may be various.

Varying the projectile nose shape not only led to significantly different ballistic limit velocity, but also altered the ballistic limit boundary, as shown in Figure 11(b). Consider first double impacts by projectiles having the same nose shape. Similar to double impacts by spherical projectiles, the ballistic limit boundary of double impacts by flat projectiles was also approximately bi-linear, while that of conical projectiles exhibited a circular arc morphology. The differences in the shape of ballistic limit boundaries were mainly attributed to differences in failure modes, as shown in Figure 12(b). When subjected to double impacts by spherical, flat and conical projectiles, the target plate exhibited secondary radial fracture after plugging, shear plugging and petalling failure, respectively. Similar failure modes were observed experimentally in aluminum alloy plates hit by projectiles having different nose shapes in the reference[35].

The ballistic limit boundaries obtained by hitting the target plate first by spherical projectile (I) and then by conical projectile (II) as well as first by conical projectile (I) and then by spherical projectile (II) were also presented in Figure 11(b), the former marked as Sphere-Cone and the latter as Cone-Sphere. Due to the combined effects of projectile nose shape and impacting sequence of projectiles having different nose shapes, it could be seen from Figure 11(b) that the size of equivelocity ballistic limit velocity was reduced in the following order: Sphere-Sphere, Flat-Flat, Sphere-Cone, Cone-Cone, Cone-Sphere. As previously mentioned, when the target plate was hit first by the conical projectile, it already experienced severe deformation such that its capability to absorb the impact energy of the follow-up spherical projectile was weakened. Consequently, the equivelocity ballistic limit velocity of Cone-Sphere double impacts was lower than that of Sphere-Cone double impacts; Figure 11(b).

4.4 Boundary condition

To understand how the boundary condition of the target plate affects its ballistic resistance, additional FE simulations were carried out for double impacts by spherical projectiles at the same location (target center), with Δt fixed at 1000 μs. As shown in Figure. 2(c), fully-fixed disc, fully-fixed square, and oppositely-fixed square having the same effective impacted area were considered, and the simulation results were presented in Figure 13. It was seen that, for the cases considered in the present study, boundary conditions had minimal influence on the ballistic limit boundary in V_I-V_{II} space. The deformation and failure modes of the target were not altered when boundary condition was varied, remained as (in order of occurrence): local bulging, propagation of plastic hinges due to bending, membrane stretching and saucer-like deformation, and finally secondary radial fracture after plugging. Moreover, this numerical result agreed well with the experimental data reported in a previous study[33], so the ballistic performance was independent of the boundary shape.

Of course, such conclusion was only preliminary and subjected to the following assumptions: Δt = 1000 μs, impacting at the target center, double impacts at the same location (no offset), the diameter of projectile (12.7 mm) much smaller than diameter/width (100 mm) of the target, and no change in projectile nose shape. For instance, if the impact position was not at the target center but offset and adjacent to the boundary of the target, its ballistic performance might be significantly different from that reported here. Clarification of this and other issues not addressed in the current investigation will be presented in a separate study.

4.5 Ballistic limit surface in V_I-V_{II}-V_{III} space

Next, the concept of ballistic limit boundary in V_I-V_{II} space was extended to V_I-V_{II}-V_{III} space to construct the ballistic limit surface. For illustration, triple impacts at the identical location of a fully-clamped disc were simulated, with the interval time between sequential impacts at 1000 μs. Figure 14(a) displayed the ballistic limit surface fitted using the method of thin-plate spline interpolation, which appeared to be approximately spherical. The intersection of this ballistic limit surface with cube diagonal was defined herein as the equivelocity ballistic limit velocity, V_{3L}. For the case considered, V_{3L} ~ 95 m s^{-1}, which is considerably smaller than the corresponding limit (121.3 m s^{-1}) of double-impact, let alone the limit (206.3 m s^{-1}) of single-impact. That is, as the number of impacts (at the same location) increased, the equivelocity ballistic limit velocity decreased. According to the pseudo-shakedown phenomenon[11,12], it can be inferred that the equivelocity ballistic limit velocity might tend to a constant as the number of impacts is increased, but this remains to be verified in the future.

In Figure 14(b), contour lines of the ballistic limit surface in V_I-V_{II} space were plotted. These contour lines were seen to be asymmetrical. For typical instance, V_{3L} = 102.5 m s^{-1} at position **A** (V_I = 145 m s^{-1} and V_{II} = 45 m s^{-1}), while V_{3L} = 88.5 m s^{-1} at position **B** (V_I = 45 m s^{-1} and V_{II} = 145 m s^{-1}).

5. Concluding remarks

Numerical simulations based on the finite element method were carried out to investigate the ballistic performance of fully-clamped 304 stainless steel plates under multiple impacts of rigid projectiles, with the equivalent plastic strain employed to define material damage and failure/fracture. For double impacts at the same location, the predicted ballistic limit velocity V_L (single impact), equivelocity ballistic limit velocity V_{2L} (double impacts), ballistic limit boundary in V_I-V_{II} space, and corresponding deformation/failure modes agreed well with existing experimental results. Subsequently, the effects of impact position, interval time between sequential impacts, the shape of projectile nose, and boundary condition on multi-hit ballistic performance, including ballistic limit velocity and deformation/failure modes, were systematically characterized. In addition, for triple impacts at the same location, the concept of ballistic limit boundary was extended to construct ballistic limit surface in V_I-V_{II}-V_{III} space. The main conclusions were summarized as follows:

i) With the impact velocity of projectile I fixed, the larger the impact position offset of projectile II, the higher the ballistic limit velocity (i.e., ballistic resistance) under double impacts.

ii) As the interval time between sequential impacts was increased, the residual velocity of projectile II increased and tended to a constant value.

iii) Due to the combined effects of projectile nose shape and impacting sequence of projectiles having different nose shapes (spherical, flat and conical), the size of equivelocity ballistic limit velocity for double impacts at the identical location was reduced, in the following order: Sphere-Sphere, Flat-Flat, Sphere-Cone, Cone-Cone, Cone-Sphere.

iv) For double impacts by spherical projectiles at target center, the ballistic limit boundary was not affected by the boundary condition of target plate.

v) For multiple impacts by spherical projectiles at the identical location, the equivelocity ballistic limit velocity decreased with the increasing number of impacts, i.e., $V_L > V_{2L} > V_{3L}$.

The results presented in this study are helpful for designing high-performance protective systems against multiple projectile impacts. It should be noted that the current study is limited to the ballistic performance of thin 304 SS plates under multiple impacts of the rigid projectiles with a fixed diameter of 12.7 mm and a fixed mass of 8.3 g. Changes in impact conditions (such as thickness and material properties of target plate, mass of impactor, etc.) may lead to considerably different phenomena and results, thus requiring further studies.

Declaration of Conflicting Interests

The author(s) declared no potential conflicts of interest with respect to the research, authorship, and/or publication of this article.

Funding

This work was supported by the National Natural Science Foundation of China (11972185, 12002156 and 11902148), the Open Fund of State Key Laboratory of Mechanics and Control of Mechanical Structures (MCMS-E-0219K02 and MCMS-I-0219K01), the Priority Academic Program Development of Jiangsu Higher Education Institution (PAPD), and the Natural Science Fund Project in Jiangsu Province of China (BK20190392).

References

1. Jacobs MJN and Van Dingenen JLJ. Ballistic protection mechanisms in personal armour. *J Mater Sci* 2001; 36: 3137-3142.
2. Seifoori S and Liaghat GH. A semianalytical and numerical study of penetration and perforation of an ogive-nose projectile into concrete targets under normal impact. *P I Mech Eng*

C-J MEC 2011; 225: 1782-1797.

3. Goel A, Uth T, Wadley HNG, et al. Effect of surface properties on momentum transfer to targets impacted by high-velocity sand slugs. *Int J Impact Eng* 2017; 103: 90-106.
4. Zhang DJ, Zhao ZY, Du SF, et al. Dynamic response of ultralight all-metallic sandwich panel with 3D tube cellular core to shallow-buried explosives. *Sci China Tech Sci* 2021; 64: 1371-1388.
5. Zhang CB, Di DN, Chen XW, et al. Characteristics structure analysis on debris cloud in the hypervelocity impact of disk projectile on thin plate. *Def Technol* 2020; 16: 299-307.
6. Heimbs S, Wagner T, Viana Lozoya JT, et al. Comparison of impact behaviour of glass, carbon and Dyneema composites. *P I Mech Eng C-J MEC* 2019; 233: 951-966.
7. Wadley HNG, Dharmasena KP, O'Masta MR, et al. Impact response of aluminum corrugated core sandwich panels. *Int J Impact Eng* 2013; 62: 114-128.
8. Zhang R, Han B and Lu TJ. Confinement effects on compressive and ballistic performance of ceramics: a review. *Int Mater Rev* 2021; 66: 287-312.
9. Boria S, Scattina A and Belingardi G. Experimental investigation on a fully thermoplastic composite subjected to repeated impacts. *P I Mech Eng C-J MEC* 2019; 233: 6985-7002.
10. Hazell PJ, Roberson CJ and Moutinho M. The design of mosaic armor: the influence of tile size on ballistic performance. *Mater Des* 2008; 29: 1497-1503.
11. Jones N. Pseudo-shakedown phenomenon for the mass loading of plating. *Int J Impact Eng* 2014; 65: 33-39.
12. Jones N. *Structural impact*. 2nd ed. Cambridge: Cambridge University Press, 2012, p.317.
13. Haque BZ, Harrington JL and Gillespie JW. Multi-hit ballistic impact on S-2 glass/SC15 thick-section composites: experiments. *J Strain Anal Eng Des* 2012; 47: 480-494.
14. Haque BZ, Harrington JL and Gillespie JW. Multi-hit ballistic impact on S-2 glass/SC15 thick-section composites: finite element analyses. *J Strain Anal Eng Des* 2012; 47: 495-512.

15. Deka LJ, Bartus SD and Vaidya UK. Multi-site impact response of S2-glass/epoxy composite laminates. *Compos Sci Technol* 2009; 69: 725-735.
16. Shen ZW, Hu DA, Zhang YM, et al. Continuous twice-impacts analysis of UHMWPE laminate fixed with bolted joints. *Int J Impact Eng* 2017; 109: 293-301.
17. Chen L, Cao MJ and Fang Q. Ballistic performance of ultra-high molecular weight polyethylene laminate with different thickness. *Int J Impact Eng* 2021; 156: 103931.
18. Kong XP, Jiang ZG, Yan LH, et al. A numerical study on adhesive layer effects and the protection capability of ceramic composite armors against multi-hit. *Gongcheng Lixue/Engineering Mechanics* 2012; 29: 251-256.
19. Shen YH, Wang YW, Du SF, et al. Effects of the adhesive layer on the multi-hit ballistic performance of ceramic/metal composite armors. *J Mater Res Technol* 2021; 13: 1496-1508.
20. de Rosset WS. Patterned armor performance evaluation. *Int J Impact Eng* 2005; 31: 1223-1234.
21. Zhao ZN, Han B, Li FH, et al. Enhanced bi-layer mosaic armor: experiments and simulation. *Ceram Int* 2020; 46: 23854-23866.
22. Ni CY, Li YC, Xin FX, et al. Ballistic resistance of hybrid-cored sandwich plates: numerical and experimental assessment. *Compos Part A - Appl S* 2013; 46: 69-79.
23. Karthikeyan K, Russell BP, Deshpande VS, et al. Multi-hit armour characterisation of metal-composite bi-layers. *J Mech Mater Struct* 2012; 7: 721-734.
24. Russell BP. Multi-hit ballistic damage characterisation of 304 stainless steel plates with finite elements. *Mater Des* 2014; 58: 252-264.
25. Kong XP, Jiang ZG and Liu F. Simulation on ceramic composite armors against multi-hit of APPs. *Appl Mech Mater* 2011; 105-107: 1648-1652.
26. Qian L and Qu M. Study on terminal effects of dense fragment cluster impact on armor plate. Part II: numerical simulations. *Int J Impact Eng* 2005; 31: 769-780.
27. Zhu L, Shi SY and Jones N. Dynamic response of stiffened plates under repeated impact. *Int J*

Impact Eng 2018; 117: 113-122.

28. LS-DYNA Support. Damping, www.dynasupport.com/howtos/general/damping (2018, accessed 13 Jun 2021).
29. Johnson GR and Cook WH. A constitutive model and data for metals subjected to large strains, high strain rates and high temperatures. In: *Proceedings of the Seventh International Symposium on Ballistics*, The Hague, The Netherlands, 1983, pp.541-547.
30. Lichtenfeld JA, Mataya MC and Van Tyne CJ. Effect of strain rate on stress-strain behavior of alloy 309 and 304L austenitic stainless steel. *Metall Mater Trans A* 2006; 37A: 147-161.
31. Rezasefat M, Mostofi TM and Ozbakkaloglu T. Repeated localized impulsive loading on monolithic and multi-layered metallic plates. *Thin Wall Struct* 2019; 144: 106332.
32. Zhang DQ, Luo L and Zhang ZY. The impact of vertical milling tool-path on the integrity of work piece surface. *Modular Machine Tool & Automatic Manufacturing Technique* 2015(9):24-27.
33. Jones N, Birch RS and Duan R. Low-velocity perforation of mild steel rectangular plates with projectiles having different shaped impact faces. *J Press Vessel - T ASME* 2008; 130: 031206.
34. Jones N and Birch RS. Low velocity perforation of mild steel circular plates with projectiles having different shaped impact faces. *J Press Vessel - T ASME* 2008; 130: 031205.
35. Raguraman M, Deb A and Jagadeesh G. A numerical study of projectile impact on thin aluminium plates. *P I Mech Eng C - J MEC* 2009; 223: 2519-2530.

List of Table and Figure captions

Table 1. Material parameters of 304 SS.[23,24,30,32]

Table 2. Comparison of ballistic limit data obtained from experiment[23], simulation[24] and this study.

Figure 1. Ballistic limit boundary in V_I-V_{II} space.[23]

Figure 2. (a) Schematic of impact location and interval time, (b) three different projectile nose shapes, and (c) three different boundary conditions of target plate.

Figure 3. Finite element model of fully-clamped plate impacted by rigid spherical projectile.

Figure 4. Fitting of material parameters for 304 SS: (a) quasi-static tensile true stress versus plastic strain curve and (b) strain rate effect.

Figure 5. Ballistic limit boundary for double impacts at the same location: comparison with existing experimental and numerical results[23,24].

Figure 6. Comparison of failure modes from single impact just below V_L between (a) experiment[23] and (b) present FE simulation. Comparison of failure modes from double impacts at V_{2L} among (c) experiment[23], (d) simulation[24], and (e) present FE simulation.

Figure 7. (a) Ballistic limit boundary for different offset distances d, (b) residual velocity of projectile II (V_I = 120 m s^{-1}), and (c) residual velocity of projectile II (V_I = 220 m s^{-1}) for selected offsets. (d) Evolution of axial and radial components of projectile II for varying offset, with V_I = 120 m s^{-1}.

Figure 8. (a) Effective plastic strain contour of target plate at t_{II} = 0 μs (i.e., just before the impact of projectile II was initiated). Evolution of equivalent plastic strain for varying impact location of projectile II (V_{II} = 140 m s^{-1}): (b) d = 0 mm, (c) d = 12.7 mm, and (d) d = 25 mm. (e) Influence of impact location of projectile II (V_{II} = 140 m s^{-1}) on failure modes of target plate. For all plotting, the impact velocity of projectile I was fixed at V_I = 120 m s^{-1}.

Figure 9. Dynamic response of the target plate during projectile I impact (V_I = 120 m s^{-1}): (a) evolution of deflection and contact force between projectile and target plate, and (b) deformation

process during the bulge phase.

Figure 10. (a) Residual velocity of projectile II versus interval time of impact Δt, with V_I = 120 m s^{-1} and V_{II} = 220 m s^{-1}. (b) Ballistic limit boundaries for Δt = 0 μs, 32 μs and 1000 μs.

Figure 11. (a) Residual velocity of projectile I having varying nose shape (single impact) and (b) effect of projectile nose shape and impact sequence of projectiles I and II having different nose shapes on ballistic limit boundary.

Figure 12. Effects of projectile nose shape on deformation and failure modes of target plate after (a) first impact and (b) second impact, with V_I = 120 m s^{-1} and V_{II} = 120 m s^{-1}.

Figure 13. Effect of boundary condition on ballistic limit boundary under double impacts at target center.

Figure 14. (a) Three-dimensional and (b) top view of ballistic limit surface in V_I-V_{II}-V_{III} space for triple impacts by spherical projectiles at the identical location.

Table 1

Parameters	**Value**
Density, ρ (kg m^{-3})	7800
Shear modulus, G (GPa)	76.9
Static yield strength, A (MPa)	287.7
Strain hardening constant, B (MPa)	583.5
Strain hardening exponent, n	0.53
Strain rate constant, C (s^{-1})	12540
Strain rate constant, P	6
Thermal softening exponent, m	0
Damage constant, D_1	0.2
Damage constant, D_2	0.76
Damage constant, D_3	- 0.95
Damage constant, D_4	0
Damage constant, D_5	0

Table 2

Source	**Ballistic limit velocity V_L (m s^{-1})**	**Prediction error for V_L (%)**	**Equivelocity ballistic limit velocity V_{2L} (m s^{-1})**	**Prediction error for V_{2L} (%)**
Experiment[23]	205.1	—	127.2	—
Simulation[24]	209.9	+ 2.3	133.6	+ 5.0
This study	206.3	+ 0.6	121.3	- 4.6

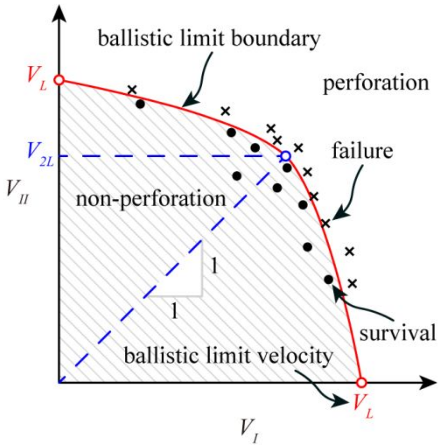
ballistic limit boundary
perforation
V_L
V_{2L}
failure
V_{II}
non-perforation
1
1
survival
ballistic limit velocity
V_L
V_I

Figure 1

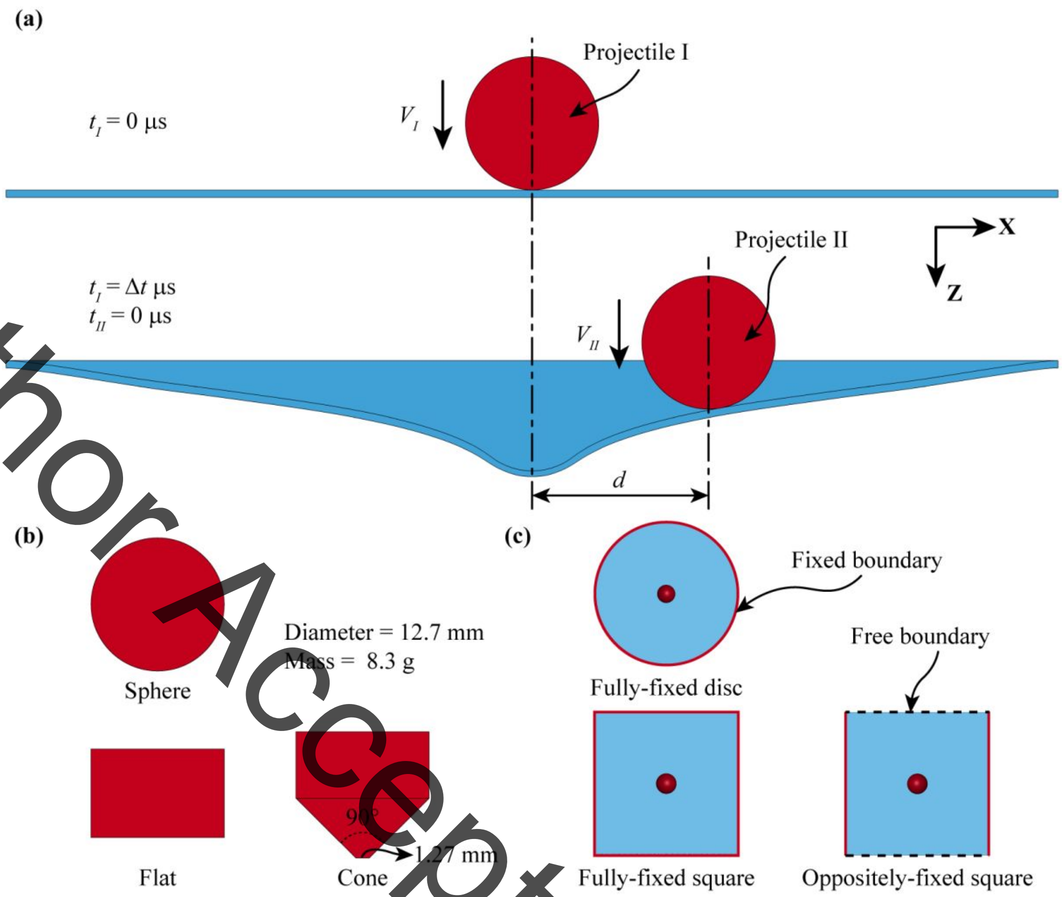
(a)
Projectile I
$t_I = 0$ μs
V_I
Projectile II
X
Z
$t_I = \Delta t$ μs
$t_{II} = 0$ μs
V_{II}
d
(b)
(c)
Fixed boundary
Diameter = 12.7 mm
Mass = 8.3 g
Sphere
Free boundary
Fully-fixed disc
90°
1.27 mm
Flat
Cone
Fully-fixed square
Oppositely-fixed square

Figure 2

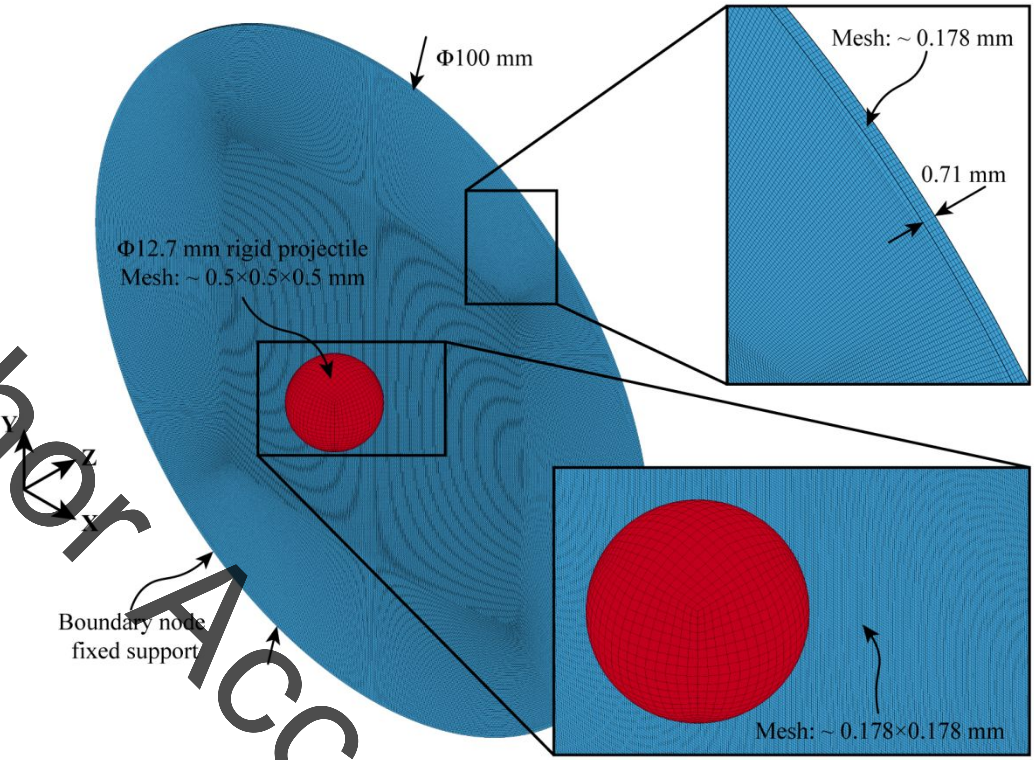
Φ100 mm
Mesh: ~ 0.178 mm
0.71 mm
Φ12.7 mm rigid projectile
Mesh: ~ 0.5×0.5×0.5 mm
Y
Z
X
Boundary node
fixed support
Mesh: ~ 0.178×0.178 mm

Figure 3

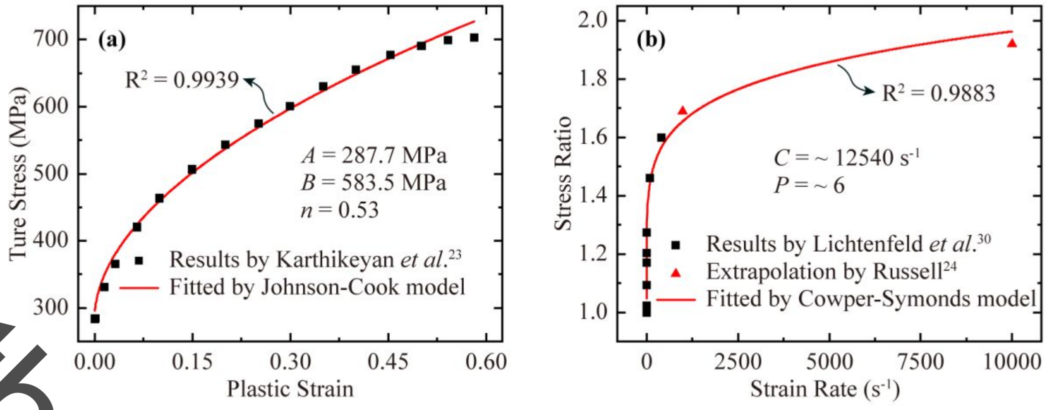
(a)
700
600
500
400
300
Ture Stress (MPa)
R² = 0.9939
A = 287.7 MPa
B = 583.5 MPa
n = 0.53
Results by Karthikeyan et al.23
Fitted by Johnson-Cook model
0.00 0.15 0.30 0.45 0.60
Plastic Strain
(b)
2.0
1.8
1.6
1.4
1.2
1.0
Stress Ratio
R² = 0.9883
C = ~ 12540 s-1
P = ~ 6
Results by Lichtenfeld et al.30
Extrapolation by Russell24
Fitted by Cowper-Symonds model
0 2500 5000 7500 10000
Strain Rate (s-1)

Figure 4

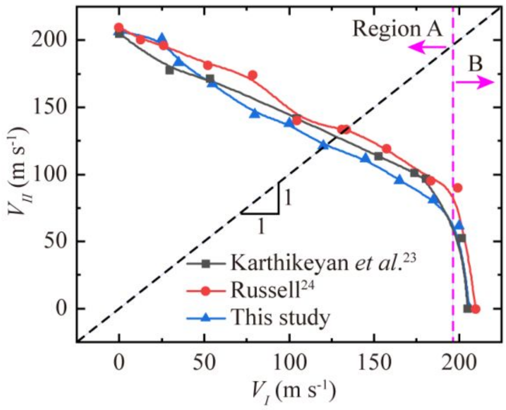
Region A
B
200
150
100
50
0
0
50
100
150
200
V_{II} (m s^{-1})
V_I (m s^{-1})
1
1
Karthikeyan et al.[23]
Russell[24]
This study

Figure 5

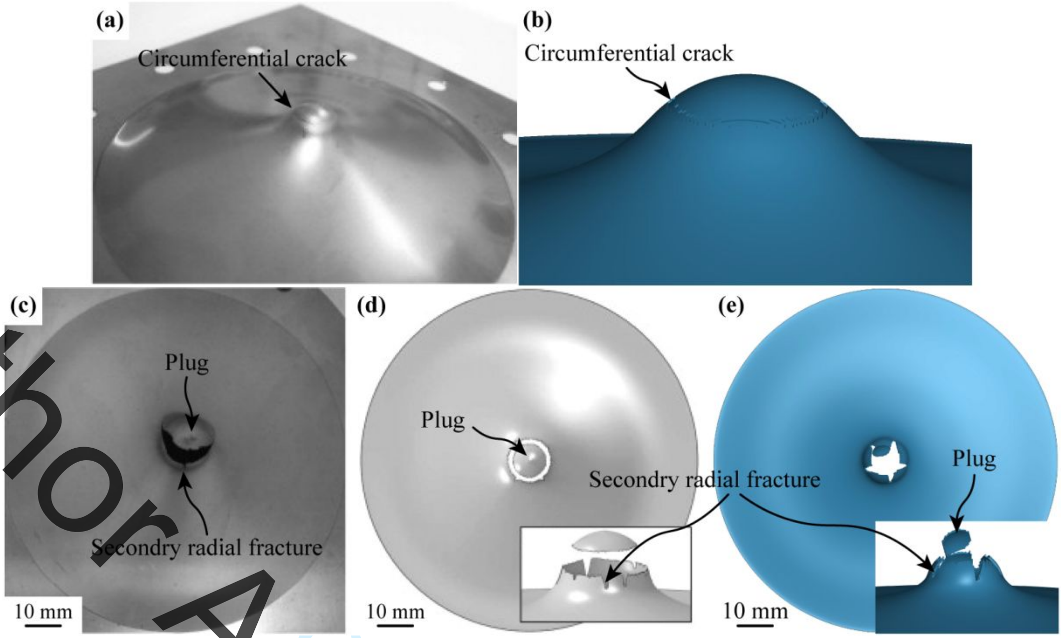
(a)
Circumferential crack
(b)
Circumferential crack
(c)
Plug
Secondry radial fracture
10 mm
(d)
Plug
Secondry radial fracture
10 mm
(e)
Plug
10 mm

Figure 6

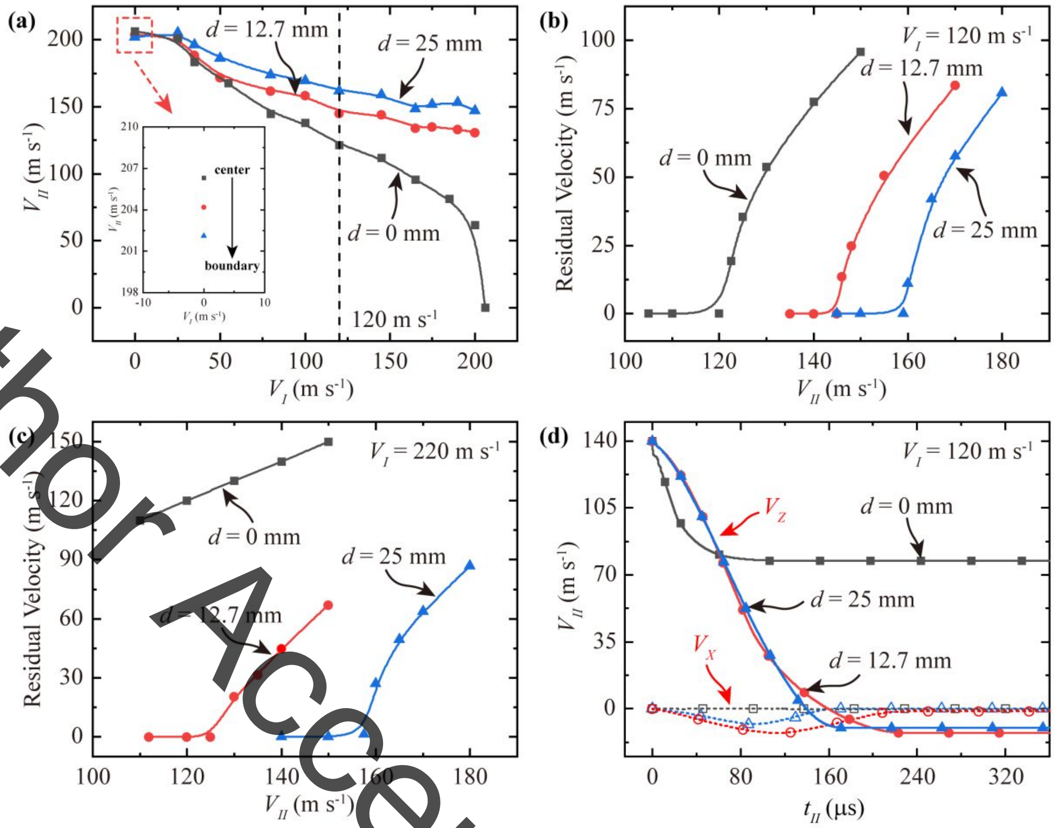
(a)
d = 12.7 mm
d = 25 mm
d = 0 mm
120 m s-1
center
boundary
V_II (m s-1)
V_I (m s-1)
(b)
V_I = 120 m s-1
d = 12.7 mm
d = 0 mm
d = 25 mm
Residual Velocity (m s-1)
V_II (m s-1)
(c)
V_I = 220 m s-1
d = 0 mm
d = 25 mm
d = 12.7 mm
Residual Velocity (m s-1)
V_II (m s-1)
(d)
V_I = 120 m s-1
V_Z
d = 0 mm
d = 25 mm
V_X
d = 12.7 mm
V_II (m s-1)
t_II (μs)

Figure 7

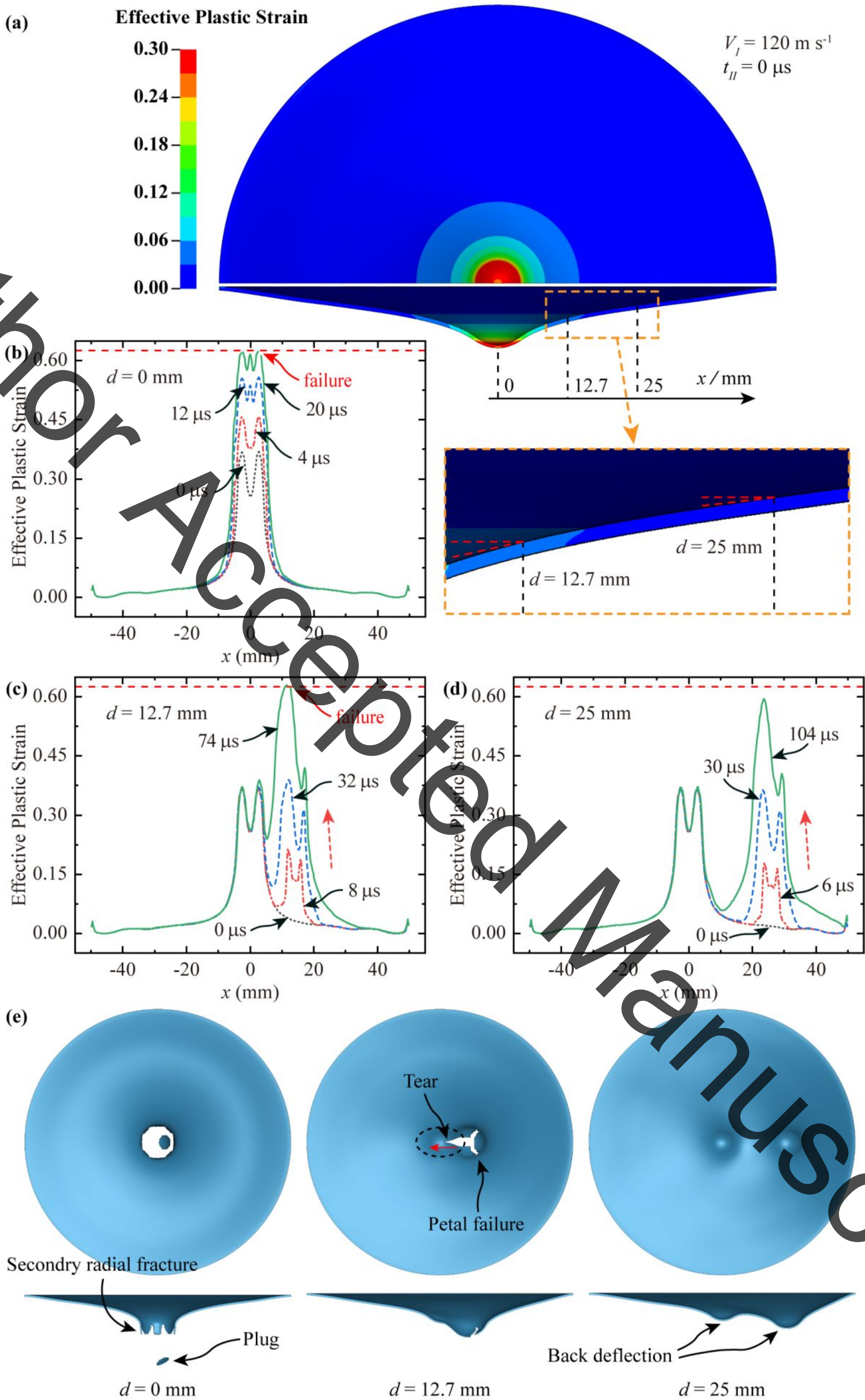
(a)
Effective Plastic Strain
0.30
0.24
0.18
0.12
0.06
0.00
V_I = 120 m s^{-1}
t_{II} = 0 μs
0
12.7
25
x / mm
d = 12.7 mm
d = 25 mm
(b)
d = 0 mm
failure
12 μs
20 μs
4 μs
0 μs
Effective Plastic Strain
x (mm)
(c)
d = 12.7 mm
failure
74 μs
32 μs
8 μs
0 μs
(d)
d = 25 mm
104 μs
30 μs
6 μs
0 μs
(e)
Tear
Petal failure
Secondry radial fracture
Plug
Back deflection
d = 0 mm
d = 12.7 mm
d = 25 mm

Figure 8

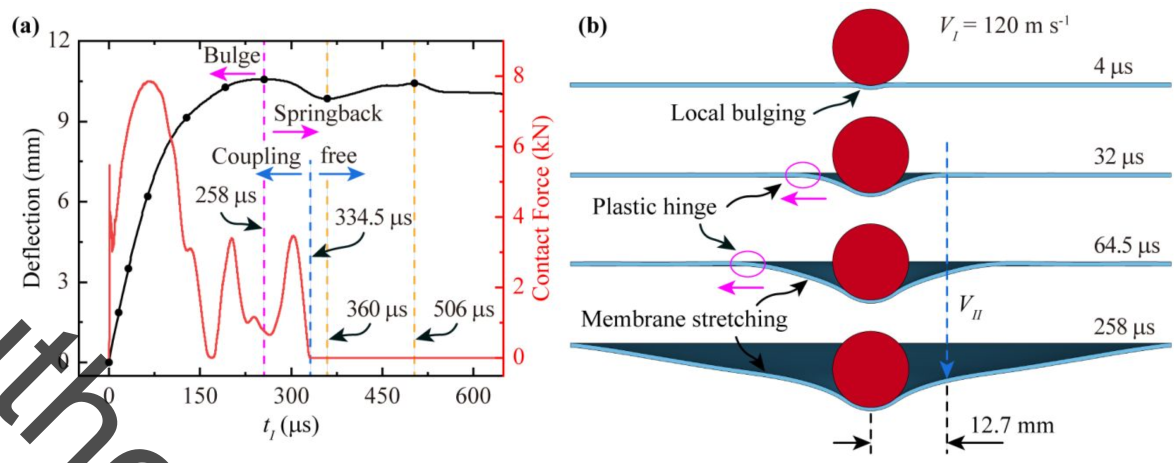
(a)
Bulge
Springback
Coupling
free
258 μs
334.5 μs
360 μs
506 μs
Deflection (mm)
Contact Force (kN)
t_I (μs)
(b)
V_I = 120 m s^{-1}
4 μs
Local bulging
32 μs
Plastic hinge
64.5 μs
Membrane stretching
V_{II}
258 μs
12.7 mm

Figure 9

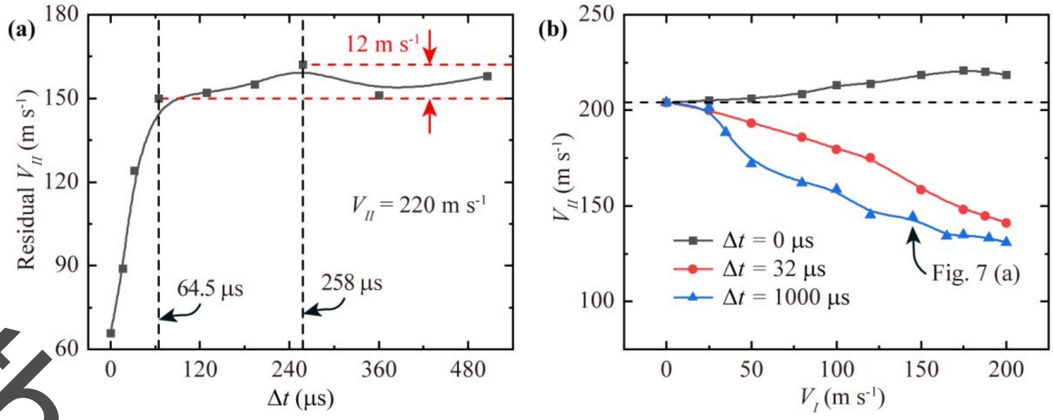
(a)
12 m s-1
Residual V_{II} (m s-1)
V_{II} = 220 m s-1
64.5 μs
258 μs
Δt (μs)
(b)
V_{II} (m s-1)
Δt = 0 μs
Δt = 32 μs
Δt = 1000 μs
Fig. 7 (a)
V_I (m s-1)

Figure 10

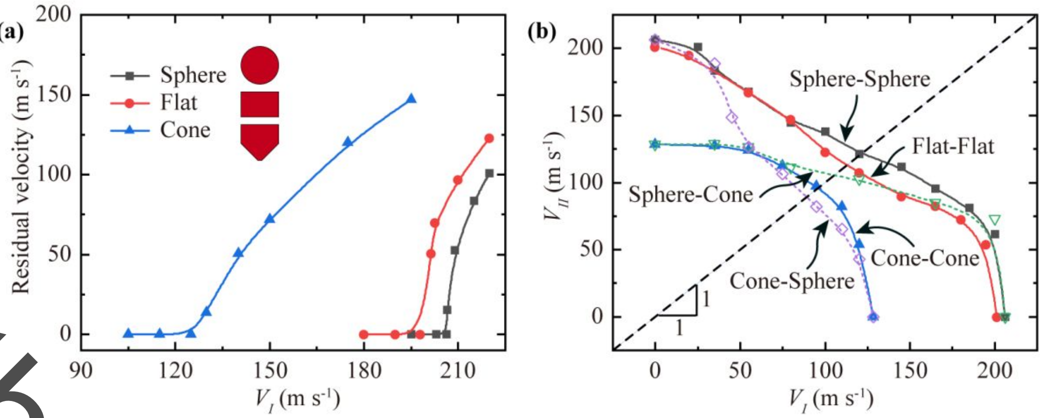
(a)
Residual velocity (m s^{-1})
Sphere
Flat
Cone
V_I (m s^{-1})
(b)
V_{II} (m s^{-1})
Sphere-Sphere
Flat-Flat
Sphere-Cone
Cone-Cone
Cone-Sphere
V_I (m s^{-1})

Figure 11

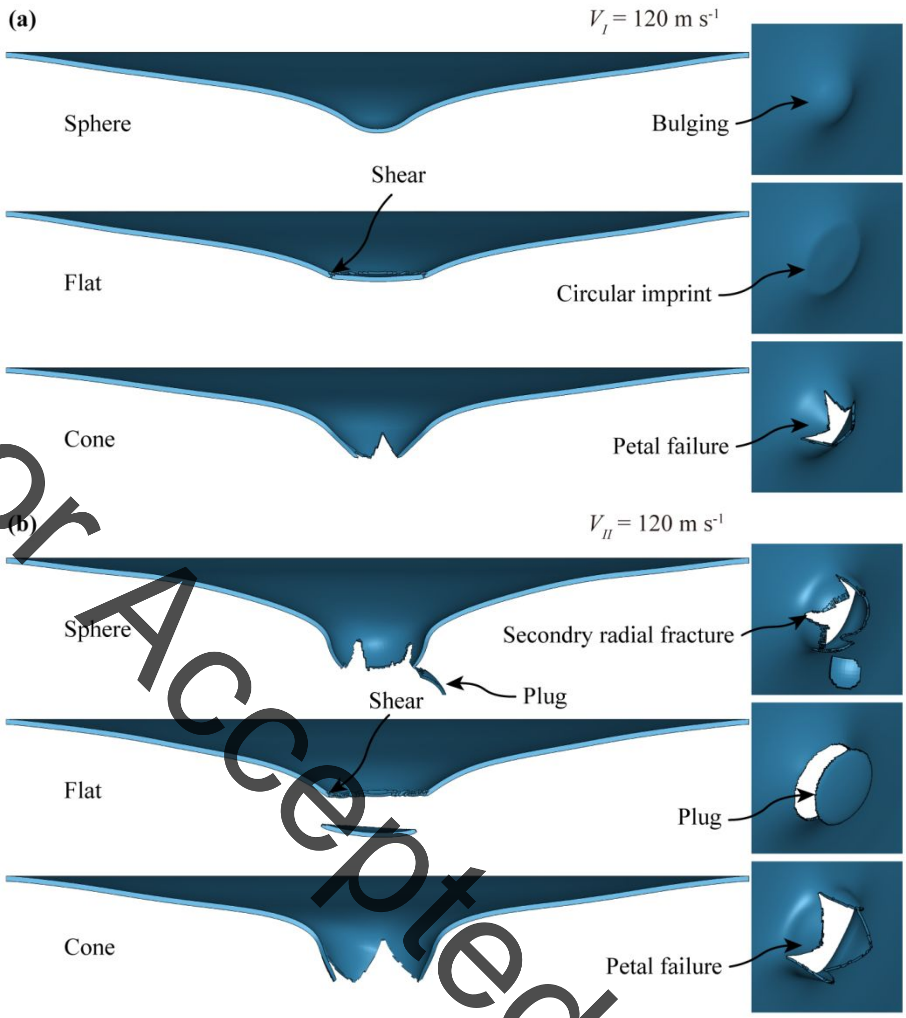
(a)
V_I = 120 m s^{-1}
Sphere
Bulging
Shear
Flat
Circular imprint
Cone
Petal failure
(b)
V_{II} = 120 m s^{-1}
Sphere
Secondry radial fracture
Plug
Shear
Flat
Plug
Cone
Petal failure

Figure 12

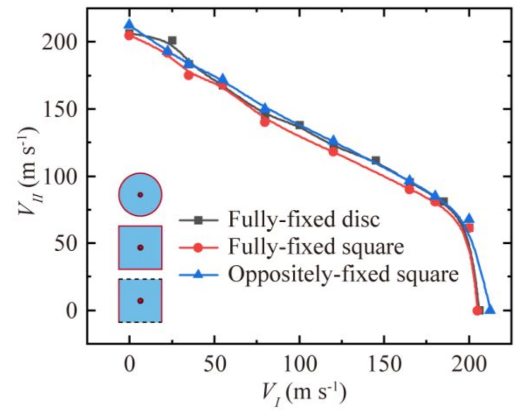
Fully-fixed disc
Fully-fixed square
Oppositely-fixed square
V_{II} (m s^{-1})
V_I (m s^{-1})
0
50
100
150
200

Figure 13

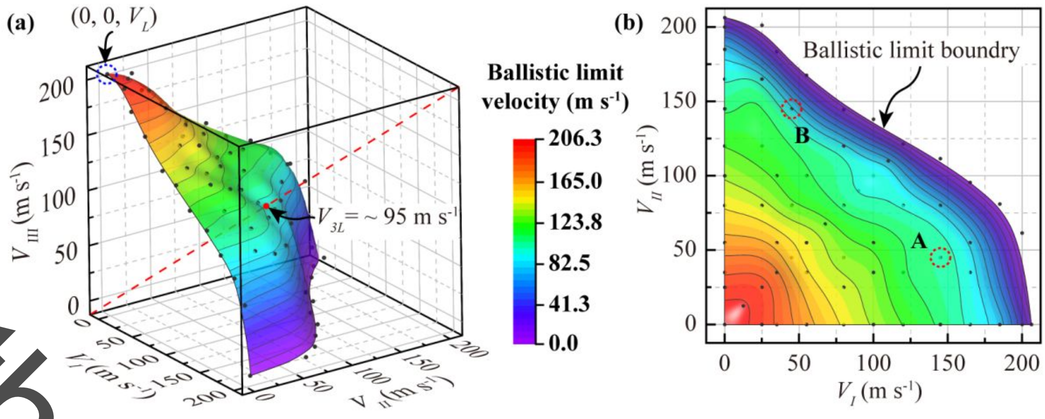
(a)
(0, 0, V_L)
V_{III} (m s^{-1})
V_{3L} = ~ 95 m s^{-1}
V_I (m s^{-1})
V_{II} (m s^{-1})
Ballistic limit velocity (m s^{-1})
206.3
165.0
123.8
82.5
41.3
0.0
(b)
Ballistic limit boundry
B
A
V_{II} (m s^{-1})
V_I (m s^{-1})

Figure 14